Available online at www.sciencedirect.com
ScienceDirect
Journal of Computational Physics 225 (2007) 1590–1602
JOURNAL OF COMPUTATIONAL PHYSICS
www.elsevier.com/locate/jcp

A new consistent splitting scheme for incompressible Navier–Stokes flows: A least-squares spectral element implementation

J.P. Pontaza *

Fluid Flow, Shell Global Solutions (US) Inc., Westhollow Technology Center, Houston, TX 77082, USA

Received 5 November 2006; received in revised form 5 February 2007; accepted 8 February 2007
Available online 20 February 2007

Abstract

This paper presents a new consistent splitting scheme for the numerical solution of incompressible Navier–Stokes flows; allowing to consistently decouple the computation of velocity and pressure. The scheme is not a pressure-correction or velocity-correction scheme, and does not display the splitting error in pressure associated with these fractional step methods. The (linearized) momentum equations are first solved based on an explicit treatment of the pressure, resulting in an advection–diffusion problem for each velocity component. A least-squares projection is used to numerically solve the advection–diffusion problem. Next, a div–curl problem is solved to make the velocity field solenoidal. This step is also handled by a least-squares projection. Finally, a pressure Poisson problem is solved to obtain the pressure field induced by the solenoidal velocity field. This is done by solving the weak Poisson problem by a Galerkin projection or alternatively by solving the strong Poisson problem by a least-squares projection. At each stage we only see coefficient matrices with a symmetric positive definite structure, and use matrix-free (preconditioned) conjugate gradient methods to numerically solve for the velocity and pressure fields. High-order C^0 spectral basis are used to span the finite element spaces. A verification benchmark shows optimal algebraic convergence rates in time for the velocity, pressure, and vorticity. The scheme is further verified by simulating the two-dimensional unsteady flow past a circular cylinder up to moderately high Reynolds numbers.

Keywords: Splitting schemes; Incompressible flow; Least-squares; Spectral/*hp* methods

1. Introduction

A major difficulty in the numerical solution of the (un-split) incompressible Navier–Stokes equations is proper velocity–pressure coupling via the incompressibility constraint. This coupling is well embodied in weak form Galerkin formulations, where the pressure is readily identified as a Lagrange multiplier enforcing the

* Tel.: +1 281 544 8015.
E-mail address: juan.pontaza@shell.com

0021-9991/$ - see front matter
doi:10.1016/j.jcp.2007.02.009

incompressibility constraint. However, at the discrete level, the velocity and pressure cannot be approximated independently due to their form of coupling and their approximation spaces must be chosen such that they satisfy a strict compatibility condition [3] (i.e. an inf–sup condition). On the other hand, least-squares formulations for incompressible flows circumvent the inf–sup condition [10], but do not naturally allow for a strong velocity–pressure coupling. The coupling is improved by using a regularized form of the incompressibility constraint [15].

An important aspect of the numerical solution of the incompressible Navier–Stokes equations is that we can split or segregate the numerical solution of the velocity and pressure fields. When formulated properly, a split approach could allow a weak form Galerkin formulation to circumvent the inf–sup condition and a least-squares formulation to avoid the use of a regularized incompressibility constraint. In spite of these attractive features, the most salient one is that, at each time step, one needs only solve a series of decoupled elliptic problems for velocity and pressure, making it very efficient for large scale numerical simulations. In this paper, we focus on developing a split approach for a least-squares formulation.

The numerical solution of the incompressible Navier–Stokes equations using least-squares finite element formulations is among the most popular applications of least-squares methods [10], and has been historically done using the coupled approach (i.e. using the un-split equations). Spectral element formulations for incompressible flows using least-squares have been presented by Proot and Gerritsma [16], Pontaza and Reddy [13], and Heinrichs [6]; where the expected exponential convergence property for smooth solutions has been demonstrated.

A review of split methods for incompressible Navier–Stokes flow is due to Guermond et al. [5], where it is shown that pressure-correction or velocity-correction fractional step schemes display a splitting error in the pressure. When using second order time stepping, the L^2 error in velocity displays the expected convergence rate of $\mathcal{O}(\Delta t^2)$ while that in pressure is only $\mathcal{O}(\Delta t)$. A rotational form of the fractional step schemes [5] is able to improve the accuracy of the pressure field to $\mathcal{O}(\Delta t^{3/2})$. Yet another approach is the consistent splitting scheme due to Guermond and Shen [4,5], where optimal $\mathcal{O}(\Delta t^2)$ convergence rates are shown in velocity and pressure for a verification benchmark. In practical applications, the consistent splitting approach due to Guermond and Shen [4] is used to post-process the pressure field obtained from a pressure-correction fractional step scheme (cf. [11]).

The objective of this paper is to present a new consistent splitting scheme for the incompressible Navier–Stokes equations. The splitting scheme is named a ''consistent scheme'' in that it is not a ''fractional step scheme'', and does not display a splitting error in the pressure. The (linearized) momentum equations are first solved based on an explicit treatment of the pressure, resulting in an advection–diffusion problem for each velocity component. Next, a div–curl problem is solved to make the velocity field solenoidal. Finally, the pressure Poisson problem with consistent Neumann boundary conditions is solved to obtain the pressure field induced by the solenoidal velocity field. At each stage we use least-squares projections to develop the finite element model. In view of the least-squares projection, we only see coefficient matrices with a symmetric positive definite structure, and use matrix-free (preconditioned) conjugate gradient (CG) methods to numerically solve for the velocity and pressure fields.

The consistent splitting scheme proposed herein differs from that proposed by Guermond and Shen [4] in that the div–curl stage to make the velocity field solenoidal is absent in their scheme and that we use least-squares projections to develop the finite element model. Numerical results using a verification benchmark show significant improvements in accuracy when using the div–curl stage to ensure a divergence-free velocity field. When using second order time stepping, the L^2 and H^1 errors in velocity, pressure, and vorticity show an ''enhanced'' convergence rate of $\mathcal{O}(\Delta t^{2+4/5})$.

An overview of the paper is as follows. In Section 2, we present the new consistent splitting scheme. In Section 3, we present its least-squares finite element formulation. Section 4 is devoted to numerical examples showing: (a) the optimal convergence property of the new consistent splitting scheme, (b) good conservation of mass properties, and (c) the applicability of the scheme to engineering-type problems. In Section 5 we present concluding remarks.

2. The consistent splitting scheme

Let $\overline{\Omega}$ be the closure of an open bounded region Ω in $\mathbb{R}^d$, where $d = 2$ or 3 represents the number of space dimensions, and $\mathbf{x} = (x_1, \ldots, x_d) = (x, y, z)$ be a point in $\overline{\Omega} = \Omega \cup \partial\Omega$, where $\partial\Omega = \Gamma$ is the boundary of Ω with unit normal $\hat{\mathbf{n}}$. The incompressible Navier–Stokes problem, in un-split form, may be stated as follows:

Find the velocity $\mathbf{u}(\mathbf{x},t)$ and pressure $p(\mathbf{x},t)$ such that

$$\frac{\partial \mathbf{u}}{\partial t} + (\mathbf{u}\cdot\nabla)\mathbf{u} + \nabla p - \frac{1}{Re}\Delta\mathbf{u} = \mathbf{0} \quad \text{in } \Omega\times(0,\tau], \tag{1}$$

$$\nabla\cdot\mathbf{u} = 0 \quad \text{in } \overline{\Omega}\times(0,\tau], \tag{2}$$

$$\mathbf{u}(\mathbf{x},0) = \mathbf{u}^0(\mathbf{x}) \quad \text{in } \Omega, \tag{3}$$

$$\mathbf{u} = \mathbf{u}_s(\mathbf{x},t) \quad \text{on } \Gamma_u\times(0,\tau], \tag{4}$$

where $\Delta = \nabla^2$, Re is the Reynolds number, $\mathbf{u}_s$ is the prescribed value of $\mathbf{u}$ on the boundary Γ_u, and in Eq. (3) the initial conditions are given. A well posed problem requires $\nabla\cdot\mathbf{u}^0 = 0$ in $\overline{\Omega}$. If $\Gamma = \Gamma_u$, the pressure may only be determined up to a constant in which case the average pressure is set to zero.

The proposed consistent splitting takes place in three stages. In the first stage, the (linearized) momentum equations are solved based on an explicit treatment of the pressure, resulting in an advection–diffusion problem for each velocity component. The resulting velocity field will, in general, not be divergence-free as the incompressibility constraint is ignored in the advection–diffusion step. In the second stage, a div–curl problem is solved to make the velocity field solenoidal. In the third and final stage, the pressure Poisson problem with consistent Neumann boundary conditions is solved to obtain the pressure field that is naturally induced by the now solenoidal velocity field.

Stage 1: Advection–diffusion step. The first step in the algorithm is essentially an advection–diffusion problem for the velocity components; it consists of seeking $\mathbf{u}^{k+1}$ such that

$$\frac{D\mathbf{u}^{k+1}}{\Delta t} + (\mathbf{u}^{k+1}_{\bigstar}\cdot\nabla)\mathbf{u}^{k+1} - \frac{1}{Re}\Delta\mathbf{u}^{k+1} = -\nabla p^{k+1}_{\bigstar}, \quad \mathbf{u}^{k+1}|_{\Gamma} = \mathbf{u}^{k+1}_s. \tag{5}$$

Note that the cartesian components of the unknown $\mathbf{u}^{k+1}$ are fully uncoupled. In Eq. (5) $D\mathbf{u}^{k+1}/\Delta t$ denotes a discrete temporal operator, and the starred quantities $\mathbf{u}^{k+1}_{\bigstar}$ and $p^{k+1}_{\bigstar}$ denote velocities and pressure fields that are extrapolated in time.

For example, for a second order BDF temporal operator $D\mathbf{u}^{k+1} = \frac{1}{2}(3\mathbf{u}^{k+1} - 4\mathbf{u}^{k} + \mathbf{u}^{k-1})$, and for a second order extrapolation in time $\mathbf{u}^{k+1}_{\bigstar} = 2\mathbf{u}^{k} - \mathbf{u}^{k-1}$. At start-up ($k = 0$), we simply use a first order temporal operator $D\mathbf{u}^{1} = \mathbf{u}^{1} - \mathbf{u}^{0}$, and first order extrapolation in time $\mathbf{u}^{1}_{\bigstar} = \mathbf{u}^{0}$. The topic of generating well-posed initial data $\mathbf{u}^0$, p^0 such that $\nabla\cdot\mathbf{u}^0 = 0$, must be respected. Here we follow the work of Marra et al. [11] to generate the well-posed initial data. It turns out that the easiest way to generate well-posed initial data is to simply use the potential flow solution as an initial condition.

Stage 2: Div–curl step. The time advanced velocity field from stage 1 will, in general, not be divergence-free. To enforce the divergence free constraint, set $\mathbf{u}^{k+1}_{\bigstar} = \mathbf{u}^{k+1}$, and solve the following div–curl problem for a solenoidal $\mathbf{u}^{k+1}$

$$\nabla\cdot\mathbf{u}^{k+1} = 0, \quad \nabla\times\mathbf{u}^{k+1} = \nabla\times\mathbf{u}^{k+1}_{\bigstar}, \quad \hat{\mathbf{n}}\cdot\mathbf{u}^{k+1}|_{\Gamma} = \hat{\mathbf{n}}\cdot\mathbf{u}^{k+1}_{\bigstar}. \tag{6}$$

Note that in this stage the starred velocity field, $\mathbf{u}^{k+1}_{\bigstar}$, no longer denotes a velocity extrapolated in time but is set to the velocity field obtained from stage 1.

Stage 3: Pressure Poisson step. Given the solenoidal velocity field $\mathbf{u}^{k+1}$ from stage 2, the pressure field p^{k+1} is obtained by solving the following pressure Poisson problem with Neumman boundary conditions of the div–curl type

$$-\nabla^2 p^{k+1} = \mathbf{u}^{k+1} : \mathbf{u}^{k+1}, \quad -\hat{\mathbf{n}}\cdot\nabla p^{k+1}|_{\Gamma} = \hat{\mathbf{n}}\cdot\left\{\frac{D\mathbf{u}^{k+1}}{\Delta t} + (\mathbf{u}^{k+1}\cdot\nabla)\mathbf{u}^{k+1} + \frac{1}{Re}\nabla\times(\nabla\times\mathbf{u}^{k+1})\right\}. \tag{7}$$

The pressure Poisson equation is obtained by taking the divergence of the momentum equations and using the incompressibility constraint to simplify it to the form shown in Eq. (7). The Neumman boundary condition is obtained by taking the inner product of the boundary unit normal with the momentum equations in its curl–curl form. The resulting div–curl form of the boundary condition is well known to give an a priori control on the divergence of the next $\mathbf{u}^{k+1}$ at the boundaries.

Alternatively, one can solve the weak form of the pressure Poisson equation; which leads to the following variational problem for the pressure field p^{k+1}

$$(\nabla q, \nabla p^{k+1}) = -\left(\nabla q, \frac{D\mathbf{u}^{k+1}}{\Delta t} + (\mathbf{u}^{k+1}\cdot\nabla)\mathbf{u}^{k+1} + \frac{1}{Re}\nabla\times(\nabla\times\mathbf{u}^{k+1})\right) \quad \forall q \in H^1(\Omega). \tag{8}$$

Weak solutions of the pressure Poisson problem may, in general, not coincide with solutions of the strong pressure Poisson problem in Eq. (7). Here we prefer to solve the strong pressure Poisson problem using a least-squares formulation, although we also consider solving the weak problem using the Galerkin approach.

3. Least-squares formulation

A least-squares formulation is chosen here to develop the finite element model of the splitting scheme for the incompressible Navier–Stokes equations described above. The reason for this is that (a) least-squares formulations have been shown to be robust for singularly perturbed advection–diffusion problems (i.e. robust in the convection dominated limit) [10], (b) least-squares formulations are optimal for div–curl problems [10], and (c) least-squares discrete problems result in linear algebraic systems with a symmetric positive definite (SPD) coefficient matrix.

The least-squares formulation is presented for an advection–diffusion problem. As we shall find out, the least-squares formulation for the equations in all the stages of the splitting scheme are special cases of this equation. We consider the linear advection–diffusion equation in dimensionless form, which can be stated as follows:

Find $\phi(\mathbf{x},t)$ such that

$$\frac{\partial\phi}{\partial t} + (\mathbf{u}_\star\cdot\nabla)\phi - \frac{1}{Pe}\nabla^2\phi = f \quad \text{in } \Omega\times(0,\tau], \tag{9}$$

$$\phi(\mathbf{x},0) = \phi^0(\mathbf{x}) \quad \text{in } \Omega, \tag{10}$$

$$\phi = \phi_s \quad \text{on } \Gamma_\phi\times(0,\tau], \tag{11}$$

$$\hat{\mathbf{n}}\cdot\nabla\phi = q_s \quad \text{on } \Gamma_q\times(0,\tau], \tag{12}$$

where $\Gamma = \Gamma_\phi\cup\Gamma_q$ and $\Gamma_\phi\cap\Gamma_q = \emptyset$, Pe is the Peclet number, $\mathbf{u}_\star$ is the prescribed velocity field, f is the source term, ϕ_s is the prescribed value of ϕ on the boundary Γ_ϕ, q_s is the prescribed normal flux on the boundary Γ_q, and in Eq. (10) the initial conditions are given.

Although direct application of least-squares variational principles to the advection–diffusion equation is possible it will result in an impractical least-squares finite element model as we would be required to work with continuously differentiable (C^1-continuous) finite element spaces. We proceed instead by first replacing the advection–diffusion problem, Eqs. (9)–(12), with its first-order system equivalent:

Find $\phi(\mathbf{x},t)$ and $\mathbf{q}(\mathbf{x},t)$ such that

$$\frac{\partial\phi}{\partial t} + (\mathbf{u}_\star\cdot\nabla)\phi - \frac{1}{Pe}\nabla\cdot\mathbf{q} = f \quad \text{in } \Omega\times(0,\tau], \tag{13}$$

$$\nabla\phi - \mathbf{q} = \mathbf{0} \quad \text{in } \Omega\times(0,\tau], \tag{14}$$

$$\nabla\times\mathbf{q} = \mathbf{0} \quad \text{in } \Omega\times(0,\tau], \tag{15}$$

$$\phi(\mathbf{x},0) = \phi^0(\mathbf{x}) \quad \text{in } \Omega. \tag{16}$$

$$\phi = \phi_s \quad \text{on } \Gamma_\phi\times(0,\tau], \tag{17}$$

$$\hat{\mathbf{n}}\cdot\mathbf{q} = q_s \quad \text{on } \Gamma_q\times(0,\tau], \tag{18}$$

where $\mathbf{q}$ is a vector valued function whose components are the fluxes of ϕ, defined in Eq. (14) and (15) is a curl constraint to ensure H^1 coercivity of the system [10].

A least-squares finite element model, where the least-squares functional is defined in terms of L^2 norms only, and is based on the equivalent first-order system, Eqs. (13)–(15), allows the use of practical and well-established C^0-continuous element expansions. The reduction in regularity requirements of the element expansions across inter-element boundaries came at the price of introducing additional independent variables, sometimes termed *auxiliary variables*. The additional variables imply an increase in cost, but can be argued to be beneficial as they may represent physically meaningful variables; fluxes in this case.

Note that the advection–diffusion problem to be solved in stage 1 of the splitting scheme is simply obtained by replacing the scalar ϕ by a velocity component and by replacing the Peclet number by the Reynolds number. Also note that the velocity gradients will be directly approximated and will be C^0-continuous across inter-element boundaries. Thus, the vorticity will be C^0-continuous across inter-element boundaries and the evaluation of its curl, $\nabla \times (\nabla \times \mathbf{u}^{k+1})$, is well defined in a finite element discretization.

Further, the Poisson problem in stage 3 is obtained by replacing the scalar ϕ by the pressure and setting $\partial/\partial t = 0$, $\mathbf{u}_\star = \mathbf{0}$, and $Pe = 1$. Finally, the *structure* of the div–curl vector problem in stage 2 is obtained (up to right-hand sides), for example, by omitting Eq. (14) and all the terms where the scalar ϕ appears and setting $Pe = 1$ and $\mathbf{q} = \mathbf{u}$. Note that in stage 2, the right-hand side of Eq. (15) with $\mathbf{q} = \mathbf{u}$ is non-zero, cf. Eq. (6).

The L^2 least-squares functional associated with the equivalent first order system of the advection–diffusion problem is

$$\mathscr{J}(\phi, \mathbf{q}; f) = \frac{1}{2}\left(\left\| \frac{D\phi^{k+1}}{\Delta t} + (\mathbf{u}_\star \cdot \nabla)\phi^{k+1} - \frac{1}{Pe}\nabla \cdot \mathbf{q}^{k+1} - f^{k+1} \right\|^2_{0,\Omega} + \|\nabla \phi^{k+1} - \mathbf{q}^{k+1}\|^2_{0,\Omega} \right.$$
$$\left. + \|\nabla \times \mathbf{q}^{k+1}\|^2_{0,\Omega} + \|\phi^{k+1} - \phi_s^{k+1}\|^2_{0,\Gamma_\phi} + \|\hat{\mathbf{n}} \cdot \mathbf{q}^{k+1} - q_s^{k+1}\|^2_{0,\Gamma_q} \right),$$

where $\|\cdot\|_0$ denotes the L^2 norm of the enclosed quantity, and it is implied that the problem will march in time for $k = 0, 1, 2, \ldots, K = \tau/\Delta t$.

Taking the first variation of the above functional with respect to ϕ and $\mathbf{q}$ and setting it to zero yields the variational form of the problem. We proceed to define a discrete problem by choosing appropriate finite element spaces for the scalar ϕ and vector components of $\mathbf{q}$. There are no restrictive compatibility conditions on the discrete spaces, so we choose the same finite element space for all primary variables. Here we use a C^0 nodal spectral basis to span the finite element spaces.

The resulting system of linear algebraic equations can be written as $\mathbf{Au} = \mathbf{b}$, where the matrix $\mathbf{A}$ is SPD, sparse, and of size $N_{\text{dof}} \times N_{\text{dof}}$, $\mathbf{u}$ represents a vector of size N_{dof} containing all the nodal unknowns, and $\mathbf{b}$ is a vector of size N_{dof}. Using the fact that the L^2 least-squares discrete system corresponds to the normal equations of a weighted collocation scheme [10,14]; where the collocation points and weights correspond to the quadrature rule points and weights used to approximate the L^2 norm integrals, we rewrite $\mathbf{Au} = \mathbf{b}$ as $\mathbf{K}^{\mathrm{T}}\mathbf{WKu} = \mathbf{K}^{\mathrm{T}}\mathbf{Wf}$. Here $\mathbf{K}$ contains the collocation residuals and is of size $N_{\text{coll}} \times N_{\text{dof}}$, $\mathbf{f}$ is a vector of size N_{coll} containing the right-hand sides of the collocation residuals, and $\mathbf{W}$ is a square matrix of size $N_{\text{coll}} \times N_{\text{coll}}$ whose diagonal entries contain the quadrature point weights.

The reasoning behind rewriting the discrete system in this manner is that we can use a suit of CG variants to solve this problem with much better numerical (finite precision) properties than when using traditional CG on $\mathbf{Au} = \mathbf{b}$. Here we use the CGLS (conjugate gradient least-squares) algorithm of Hestenes and Stiefel [9] or the LSQR (least-squares QR) algorithm by Paige and Saunders [12] on $\mathbf{K}^{\mathrm{T}}\mathbf{WKu} = \mathbf{K}^{\mathrm{T}}\mathbf{Wf}$, implemented in matrix-free form with a Jacobi preconditioner. All three algorithms (CG, CGLS, and LSQR) are analytically equivalent but the performance of CGLS and LSQR is much better in finite precision [1,12]. Comparisons of convergence speed and accuracy when using CG, CGLS, and LSQR on least-squares problems with low and high condition numbers are well documented in the study by Bjorck et al. [1]. We recommend CGLS, as it has a lower operation count than LSQR and achieves almost identical accuracy.

4. Numerical examples

4.1. Verification

In this first numerical example we wish to establish the temporal accuracy of the consistent splitting scheme, which we conjecture; should correspond to the second-order accuracy of the time integration scheme. To this end we consider a unit square $\overline{\Omega} = [0.0, 1.0] \times [0.0, 1.0]$ with Dirichlet velocity boundary data. We take the exact solution to the incompressible Navier–Stokes equations to be of the form:

$$
\begin{aligned}
u(x,y,t) &= \pi \sin^2(\pi x)\sin(2\pi y)\sin(t),\\
v(x,y,t) &= -\pi \sin^2(\pi y)\sin(2\pi x)\sin(t),\\
p(x,y,t) &= \cos(\pi x)\sin(\pi y)\sin(t).
\end{aligned}
\tag{20}
$$

The prescribed velocity field is, by construction, solenoidal and the source term $\mathbf{f}$ of the momentum equations is such that Eq. (20) is the exact solution. This "manufactured solution" is the one used in the work of Guermond and collaborators [4,5], to establish the temporal accuracy of splitting schemes.

The domain is spatially discretized using a 4×4 uniform quadrilateral finite element mesh. In each element we use 8th order nodal expansions (in each spatial direction), which is sufficient to represent the spatial variation of the analytic solution to within approximately 10^{-8} in the L^2 norm. Therefore any errors higher than this can be expected to be due to temporal accuracy. For the computations we use the full Navier–Stokes equations (i.e. with the convection terms) and set the Reynolds number to 100. The exact solution, given by Eq. (20), is used to prescribe the initial data and Dirichlet velocity boundary conditions on the entire boundary.

The time evolution of the fields is computed for $t \in [0, 10]$ for decreasing time step sizes. The L^2 error and H^1 error in velocities, pressure, and vorticity is recorded at $t = 5$ and plotted in Figs. 1 and 2 as a function of the time step size in a log–log scale.

A major finding is that, contrary to our expectations, the errors *did not* decay at an algebraic rate of order 2, as expected for the second-order accurate time marching scheme. Instead, we see a *faster* algebraic convergence rate of order 2.8 in the L^2 and H^1 norms for all field variables. Indeed, we see from Figs. 1 and 2 that the slope of the convergence curves is close to 3rd order.

At the moment, we are not able to fully explain the increase in convergence rate from the expected $\mathcal{O}(\Delta t^2)$ to the observed $\mathcal{O}(\Delta t^{2+4/5})$; but the enhanced convergence rate is certainly welcomed. The observed enhanced convergence rate may be a result of the sequence of least-squares projections performed on the velocity field, and not necessarily inherent to the splitting scheme itself. For clarity, we present below the definitions used to compute the L^2 error and H^1 error at each time step.

$$
\|w - w^{hp}\|_{L^2(\Omega)} = \left(\int_\Omega |w - w^{hp}|^2 \, \mathrm{d}\Omega \right)^{\frac{1}{2}}, \tag{21}
$$

$$
\|w - w^{hp}\|_{H^1(\Omega)} = \left(\int_\Omega |w - w^{hp}|^2 + \left| \frac{\partial w}{\partial x} - \frac{\partial w^{hp}}{\partial x} \right|^2 + \left| \frac{\partial w}{\partial y} - \frac{\partial w^{hp}}{\partial y} \right|^2 \mathrm{d}\Omega \right)^{\frac{1}{2}}. \tag{22}
$$

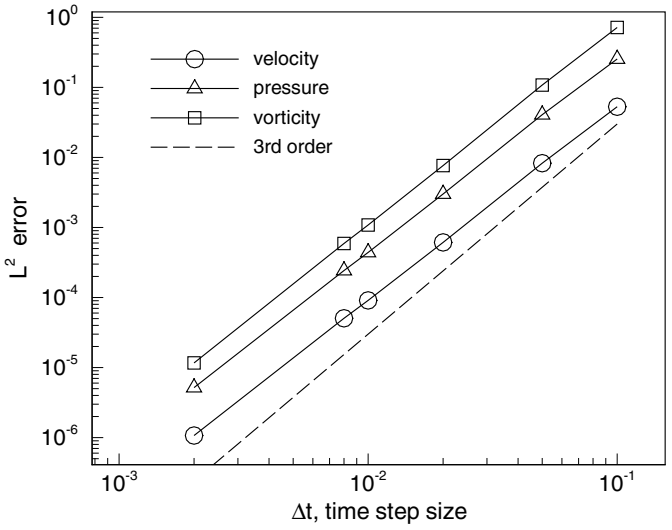

Fig. 1. Convergence of the velocity, pressure, and vorticity fields at $t = 5$ in the L^2 norm for decreasing time step sizes.

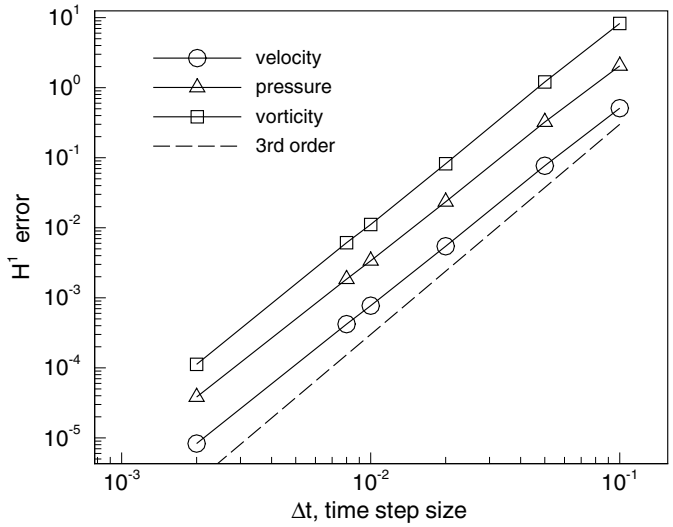

Fig. 2. Convergence of the velocity, pressure, and vorticity fields at $t = 5$ in the H^1 norm for decreasing time step sizes.

When the div–curl stage is made absent we observe an increase in the error for all field variables. To show the effect of removing the div–curl stage in the proposed splitting scheme, we plot in Fig. 3 the time history of the L^2 norm of the divergence of the velocity field with and without the div–curl stage (using $\Delta t = 0.01$). We see that when the div–curl stage is absent, the L^2 norm of the divergence of the velocity field is around four orders of magnitude higher; as there is no explicit constraint that the velocity field remain divergence-free. Similarly, we show in Fig. 4 the adverse effect of removing the div–curl stage by plotting the L^2 error of the pressure field in time (using $\Delta t = 0.01$). When the div–curl stage is absent, the L^2 error in pressure is two orders of magnitude higher. Clearly, the div–curl stage is vital in the proposed splitting scheme.

We note that the exact same convergence rates and error values were obtained when solving the weak pressure Poisson problem by a Galerkin projection or when solving the strong pressure Poisson problem by a least-squares projection. However, when using the weak pressure Poisson problem to solve for the pressure field using a Galerkin projection, the div–curl stage could not be removed to obtain reasonably accurate results.

To give the reader an idea of the cost associated with time advancing the fields by a single time step using the proposed splitting scheme, we present in Table 1 the conjugate gradient iteration count associated with

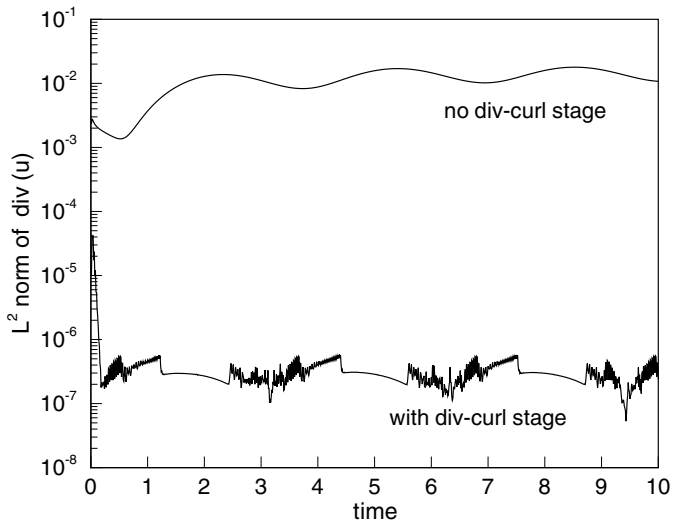

Fig. 3. Time history of the L^2 norm of the divergence of the velocity field with and without the div–curl stage.

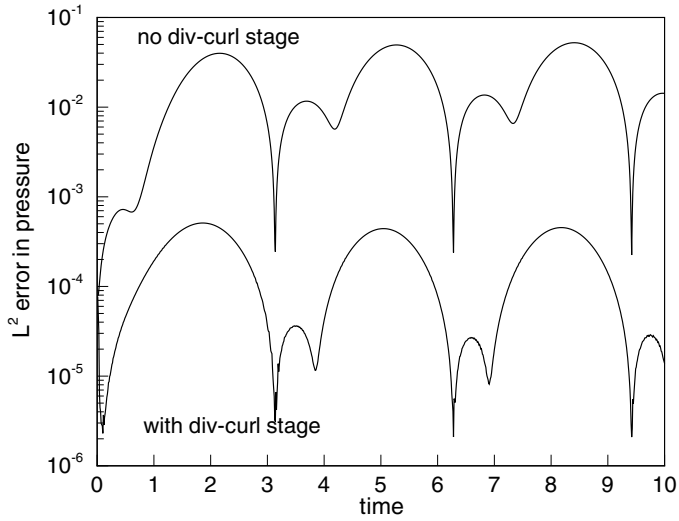

Fig. 4. Time history of the L^2 error in pressure with and without the div–curl stage.

Table 1
Conjugate gradient iteration count at each stage of the splitting scheme for a single time step

Δt	Advection–diffusion step		Div–curl step	Poisson step (weak Galerkin)	Poisson step (least-squares)
	u-velocity	v-velocity			
0.10	1543	1539	434	230	730
0.05	1338	1342	379	215	661
0.02	1194	1201	294	178	507
0.01	1083	1085	229	96	408

Residual tolerance set to 10^{-8}.

each stage for selected time step sizes. The residual tolerance for the conjugate gradient algorithm was set to 10^{-8} for this verification exercise. We see that the most expensive stage is the advection–diffusion step for the velocity components, and that the number of conjugate gradient iterations till convergence reduces with decreasing time step size for all stages. We also see that performing the Poisson step using a least-squares projection is more expensive than using a Galerkin projection for the weak Poisson problem.

4.2. A model problem to test conservation of mass

This is a model problem where a circular cylinder of unit diameter, D, is moving in a narrow channel of height $1.5D$, and is used here to test for conservation of mass. This model problem was originally proposed by Chang and Nelson [2] to test for conservation of mass using the (steady) Stokes equations. Here we present

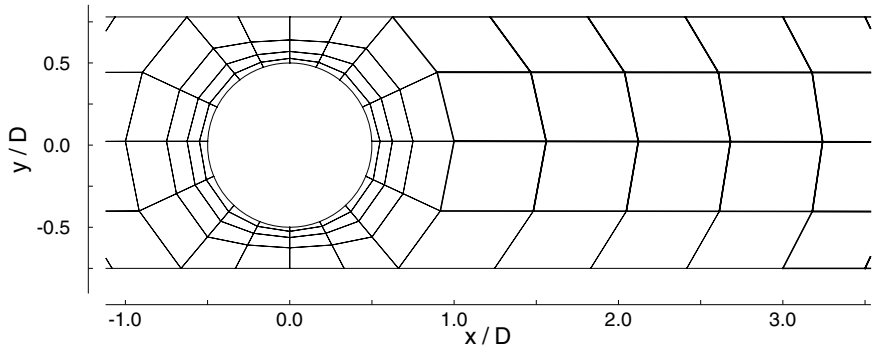

Fig. 5. Partial view of the computational domain and mesh for the model problem to test for conservation of mass.

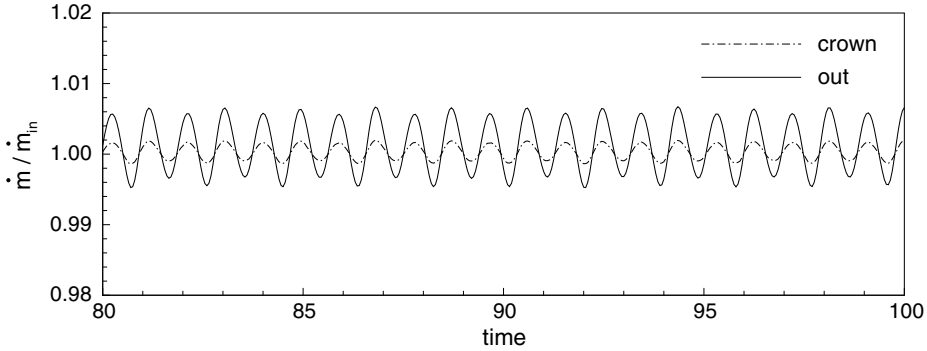

Fig. 6. Time histories of mass flow rates at the crown of the cylinder and outlet of the channel.

results for unsteady flow governed by the Navier–Stokes equations, to test for conservation of mass in time using the proposed splitting scheme.

The geometry used by Chang and Nelson [2] is slightly modified here by shifting the upper channel wall by 0.03 units to promote the desired unsteadiness and by moving the outflow boundary 5.0 units further downstream to allow the unsteady wake to become well-developed. The finite element mesh consists of 140 quadrangles and a partial view is shown in Fig. 5. The boundary conditions are $u = 1$, $v = 0$ at the upstream and lateral boundaries and no-slip boundary conditions, $u = v = 0$, at the cylinder surface. For the outflow bound-

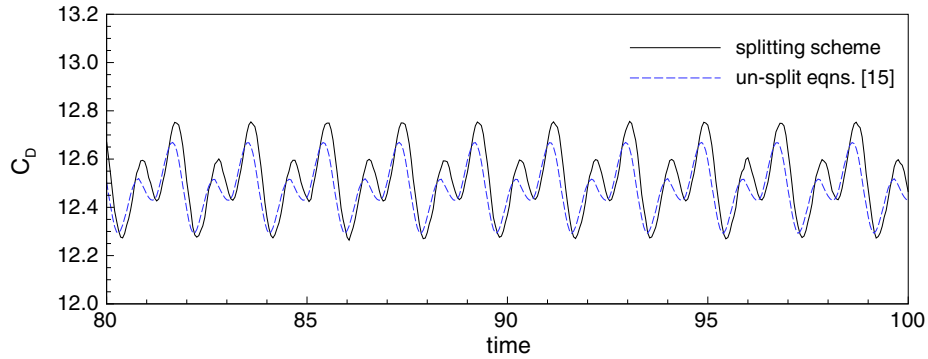

Fig. 7. Time history of drag coefficient. Comparison with drag coefficient time history obtained using the un-split Navier–Stokes equations [15].

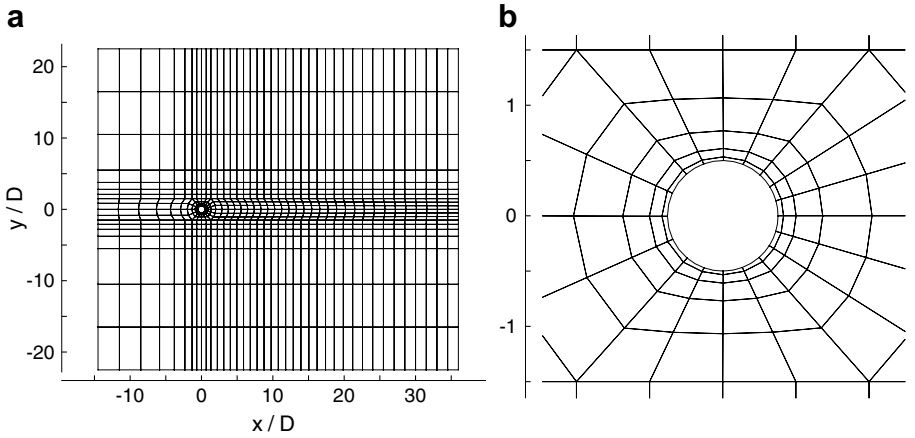

Fig. 8. Computational domain and mesh for flow past a circular cylinder. (a) Finite element mesh. (b) Close-up view of the element distribution around the surface of the circular cylinder.

ary whose unit normal is aligned with the x-axis, the outflow boundary conditions are imposed as $\partial u/\partial x = 0$, $\partial v/\partial x = 0$ in stage 1 of the splitting scheme, and as $p = 0$ in stage 3 of the splitting scheme.

The Reynolds number considered is $Re = 100$. Mass flow rates are computed at the crown of the cylinder, where the gap between the channel walls and cylinder surface is the smallest, and at the outflow of the channel.

Time histories of the mass flow rates are plotted in Fig. 6 when using a spatial resolution of p-level 6. The response is plotted for $t \in [80, 100]$, by which time the flow field is well-developed and has reached an unsteady periodic behavior. The expected response is $\dot{m}_x/\dot{m}_{\text{in}} = 1.0$ at all times. Note that the scale on which the mass flow rates are plotted allows for a maximum deviation of $\pm 2.0\%$ mass loss/gain. The splitting scheme displays good conservation of mass in time, showing oscillations of $\pm 0.4\%$ mass loss/gain in time at the crown of the cylinder and $\pm 0.6\%$ mass loss/gain in time at the outlet of the channel. Increasing the spatial resolution to a p-level of 8 and/or decreasing the time step size did not worsen or improve the conservation of mass response in time, and the same small mass loss/gains in time were observed.

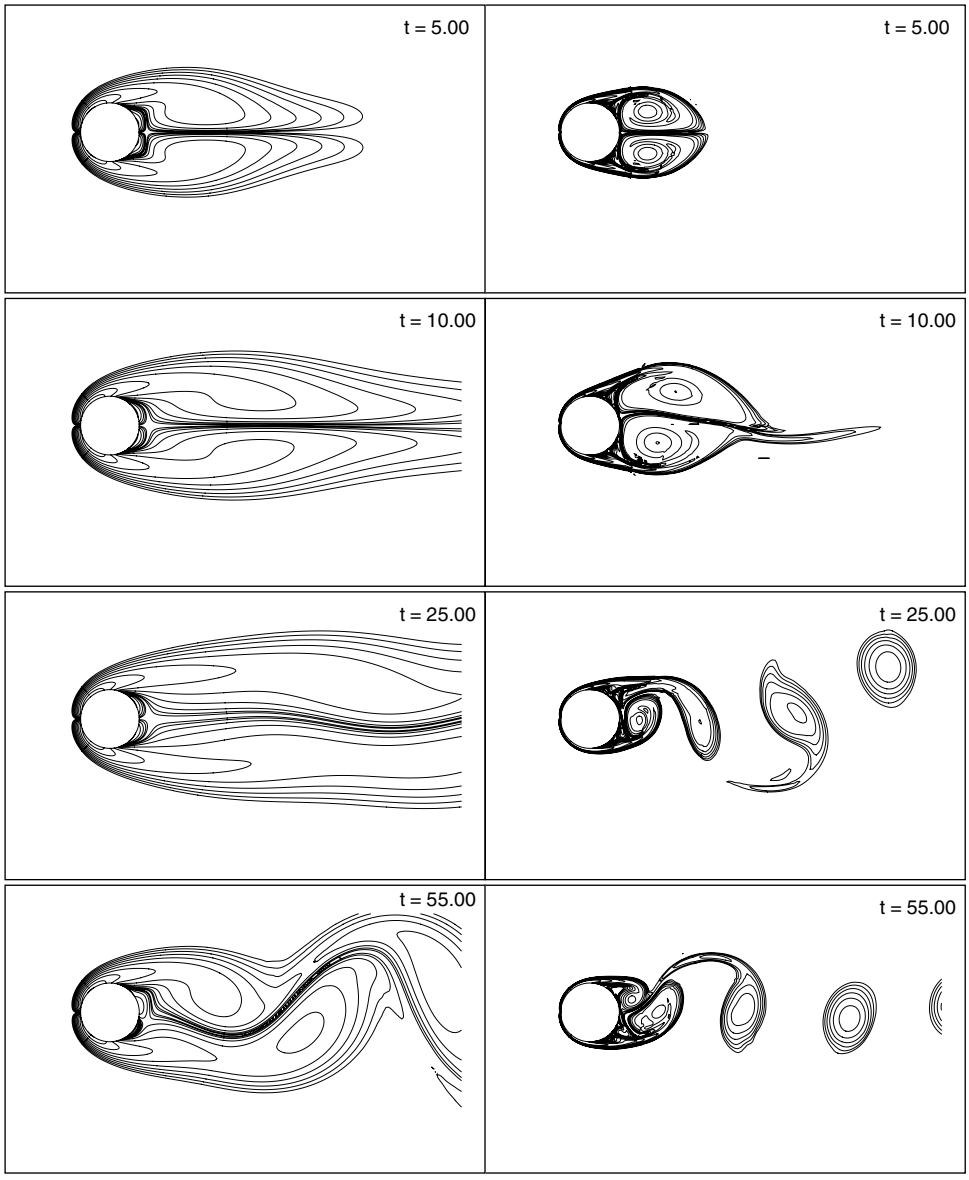

Fig. 9. Instantaneous vorticity contours at different instants in time for an impulsive start of flow past a circular cylinder. Left column $Re = 100$. Right column $Re = 10^3$.

Fig. 7 compares the time history of the drag coefficient on the circular cylinder computed using the proposed splitting scheme with that obtained using the un-split equations; reported in our previous work [15]. We see good agreement between the two responses in terms of amplitude and phase.

4.3. Unsteady flow past a circular cylinder

We consider the two-dimensional flow of an incompressible fluid past a circular cylinder. Having demonstrated optimal convergence rates in time and good conservation of mass for the proposed splitting scheme, the focus of this last numerical example is to demonstrate the accuracy of computed pressure metrics and stability of the formulation with respect to moderately high Reynolds number flow conditions.

The finite element mesh used for the computations is shown in Fig. 8, and is the one used in our previous work [15] where we reported results using the un-split equations. The size of the computational domain is taken sufficiently large to preclude unwanted effects on computed flow metrics due to blockage, or location of inflow and outflow boundaries. The circular cylinder is of unit diameter, with its center at $(x, y) = (0, 0)$, and is placed in the rectangular region $\overline{\Omega} = [-14.5, 36.0] \times [-22.5, 22.5]$. The Reynolds number is based on the free-stream velocity and cylinder diameter.

Simulations were performed for various Reynolds numbers in the range $Re \in [100, 10^3]$, at a p-level of 6 and using a time step size of $\Delta t = 0.05$. The chosen time step size allows for adequate temporal resolution, resulting in over 120 time steps per shedding cycle at $Re = 100$ and over 80 time steps per shedding cycle at $Re = 10^3$. We choose to start the simulations at each Reynolds numbers using an impulsively started flow. We follow the work of Marra et al. [11] to generate the well-posed initial data.

Although the flow is three-dimensional in nature for $Re > 188$ [7], a two-dimensional simulation is still of interest in theoretical fluid mechanics. Flow metrics such as the mean drag and base pressure coefficients are over-predicted in two-dimensional simulations due to omission of spanwise wake effects with short correlation lengths.

Fig. 9 shows instantaneous vorticity contours at different instants in time during the impulsive start of the flow, for $Re = 100$ (left column) and $Re = 10^3$ (right column). At $t = 5.0$ the flow is symmetric, but as time progresses it becomes asymmetric due to shear-layer instabilities. As expected, the higher Reynolds number flow is more susceptible to these instabilities and the shedding begins at earlier times, with a narrower wake, when compared to the lower Reynolds number flow.

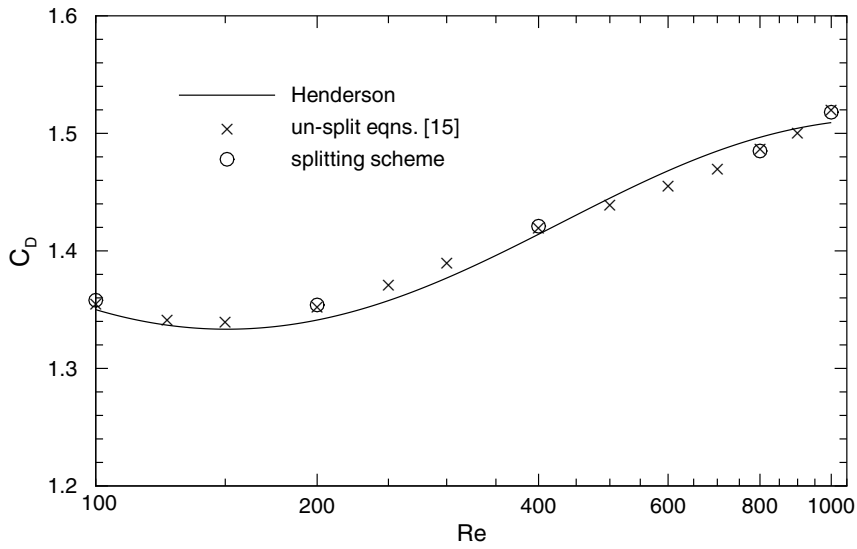

Fig. 10. Mean drag coefficient vs. Reynolds number for unsteady flow past a circular cylinder. Comparison of our 2-D simulation results with the 2-D simulation results of Henderson [7] and our 2-D simulation results using the un-split equations [15].

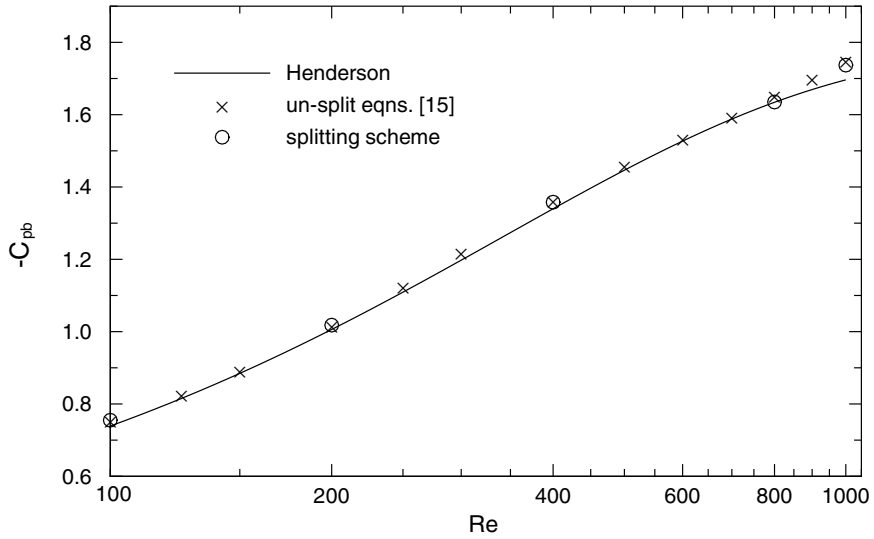

Fig. 11. Mean base pressure coefficient vs. Reynolds number for unsteady flow past a circular cylinder. Comparison of our 2-D simulation results with the 2-D simulation results of Henderson [7] and our 2-D simulation results using the un-split equations [15].

Fig. 10 shows the computed time-averaged drag coefficients and Fig. 11 the computed time-averaged base pressure coefficients for increasing Reynolds numbers. The reference curve with which we compare our simulation results represents a smooth fit to the discrete set of two-dimensional simulation data points by Henderson [7], who used a fractional step high-order method to split the Navier–Stokes equations [8]. Alongside this data, we also plot some of our earlier results [15], using the un-split equations. Overall, our simulation results using the proposed consistent splitting scheme show good agreement with the reference data over the range of Reynolds numbers considered.

5. Summary and concluding remarks

We presented a new consistent splitting scheme for the numerical solution of incompressible Navier–Stokes flows; allowing to consistently decouple the computation of velocity and pressure. Our consistent splitting scheme differs from others in a major way in that a div–curl stage enforces the divergence-free condition on the velocity field during the time marching procedure. Numerical results using a verification benchmark show significant improvements in accuracy when using the div–curl stage in the consistent splitting. When using second order time stepping, the L^2 and H^1 errors in velocity, pressure, and vorticity show an "enhanced" convergence rate of $\mathcal{O}(\Delta t^{2+4/5})$. Numerical results for problems of the inflow/outflow type show good conservation of mass and good accuracy in pressure metrics.

References

[1] A. Bjorck, T. Elfving, Z. Strakos, Stability of conjugate gradient and Lanczos methods for linear least-squares problems, SIAM J. Matrix Anal. Appl. 19 (1998) 720–736.
[2] C.L. Chang, J.J. Nelson, Least-squares finite element method for the Stokes problem with zero residual of mass conservation, J. Numer. Anal. 34 (1997) 480–489.
[3] V. Girault, P. Raviart, Finite Element Methods for Navier–Stokes Equations, Springer, Berlin, 1986.
[4] J.L. Guermond, J. Shen, A new class of truly consistent splitting schemes for incompressible flows, J. Comput. Phys. 192 (2003) 262–276.
[5] J.L. Guermond, P. Minev, J. Shen, An overview of projection methods for incompressible flows, Comput. Methods Appl. Mech. Eng. 195 (2006) 6011–6045.
[6] W. Heinrichs, Least-squares spectral collocation for the Navier–Stokes equations, J. Sci. Comput. 21 (2004) 81–90.
[7] R.D. Henderson, Details on the drag curve near the onset of vortex shedding, Phys. Fluids 7 (1995) 2102–2105.

[8] R.D. Henderson, G.E. Karniadakis, Unstructured spectral element methods for simulation of turbulent flows, J. Comput. Phys. 122 (1995) 191–217.
[9] M.R. Hestenes, E. Stiefel, Methods of conjugate gradients for solving linear systems, J. Res. Nat. Bur. Stds. B 49 (1952) 409–436.
[10] B.N. Jiang, The Least-squares Finite Element Method, Springer, New York, 1998.
[11] A. Marra, A. Mola, L. Quartapelle, L. Riviello, Calculation of impulsively started incompressible viscous flow, Int. J. Numer. Meth. Fluids 46 (2004) 877–902.
[12] C.C. Paige, M.A. Saunders, LSQR: an algorithm for sparse linear equations and sparse least-squares, ACM Trans. Math. Software 8 (1982) 43–71.
[13] J.P. Pontaza, J.N. Reddy, Spectral/*hp* least-squares finite element formulation for the Navier–Stokes equations, J. Comput. Phys. 190 (2003) 523–549.
[14] J.P. Pontaza, J.N. Reddy, Least-squares finite element formulations for viscous incompressible and compressible fluid flows, Comput. Methods Appl. Mech. Eng. 195 (2006) 2454–2494.
[15] J.P. Pontaza, A least-squares finite element formulation for unsteady incompressible flows with improved velocity–pressure coupling, J. Comput. Phys. 217 (2006) 563–588.
[16] M.M.J. Proot, M.I. Gerritsma, Least-squares spectral elements applied to the Stokes problem, J. Comput. Phys. 181 (2002) 454–477.